Final report

Investigating the intratumoral distribution of antiangiogenic and chemotherapeutic agents in primary tumors and their pulmonary metastases

Scientific background

A frequent and poor prognostic event in the progression of malignant tumors is the appearance of lung metastases. Although these patients often receive antiangiogenic (AA) agents in combination with chemotherapy, the efficacy of these combinations remains far behind the expectations that were predicted according to the results of preclinical animal studies and, moreover only a few months overall survival benefit can be achieved in cancer patients receiving AA agents.

The vascular network of tumors can be formed by various mechanisms, of which the best known is endothelial sprouting. There are also so-called alternative vascularization mechanisms (e.g., vessel incorporation or cooption and intussusctive angiogenesis) [1], that do not require endothelial cell proliferation. AA agents that are applied in the clinic are designed to inhibit the mechanism of endothelial sprouting. Moreover, preclinical studies most commonly use subcutaneously implanted tumor xenografts to model tumor growth, and these are most commonly characterized by sprouting angiogenesis.

In contrast, in highly vascularized organs (lung, liver, brain), the process of vessel co-option ("VCO") is of greater importance than sprouting angiogenesis [2-6]. Since these organs are also the most common sites of metastasis of solid tumors, we hypothesized that primary and metastatic tumors may use distinct mechanisms to form their vascular network, and thus differentially respond to AA therapy.

Aims

As a continuation of our two recent publications [7, 8], in the present study our aim was to compare the efficacy of an AA agent, sunitinib in primary and metastatic mouse models of breast, colon and renal cell tumors, using a modern tissue imaging technique (Matrix-assisted laser desorption/ionization Mass Spectrometry Imaging, MALDI-MSI) combined with immunofluorescence microscopy.

Results

For our experiments we selected the following cell lines:

- breast cancer: 4T1 (mouse)- MDAMB231 (human)
- colon cancer: C26 (mouse)- HT29 (human)
- kidney cancer: RENCA (mouse)- CAKI-2 (human)

To test the effect of sunitinib on the growth of primary tumors, cells were inoculated subcutaneously (sc.) in case of 4T1 (10^6), MDAMB231 (10^7), C26 ($5x10^5$) and HT29 (10^7) and into the kidney in case of RENCA ($5x10^4$) and CAKI-2 ($1.5x10^6$). Groups of 10 female SCID or Balb/C mice were treated daily with 80 mg/kg sunitinib-malate suspended in 1.5% carboxymethycellulose (CMC) or 1.5% CMC as vehicle agent for 2x5 days with 2 days rest in between. To assess intratumoral hypoxia and detect proliferating cells a bolus of intraperitoneal. pimonidazole (60 mg/kg), and bromo-dezoxiuridine (BrdU, 200 mg/kg) was administered 1.5 hours before the mice were sacrificed. Three hours after the last sunitinib treatment, blood was drawn from the canthus and mice were sacrificed. Tumors and normal organs were removed, tumor weight was measured and samples were snap frozen by submerging the tissues into dry ice cooled isopentane. Frozen tissues were stored at -80 oC until utilization.

As shown in Figure 1. significant tumor growth inhibition was observed in all primary models when comparing the volume of control and sunitinib treated tumors (4T1: p=0,0011; MDAMB231: p=0,0029; C26: p=0,014; HT29: p=0,0011).

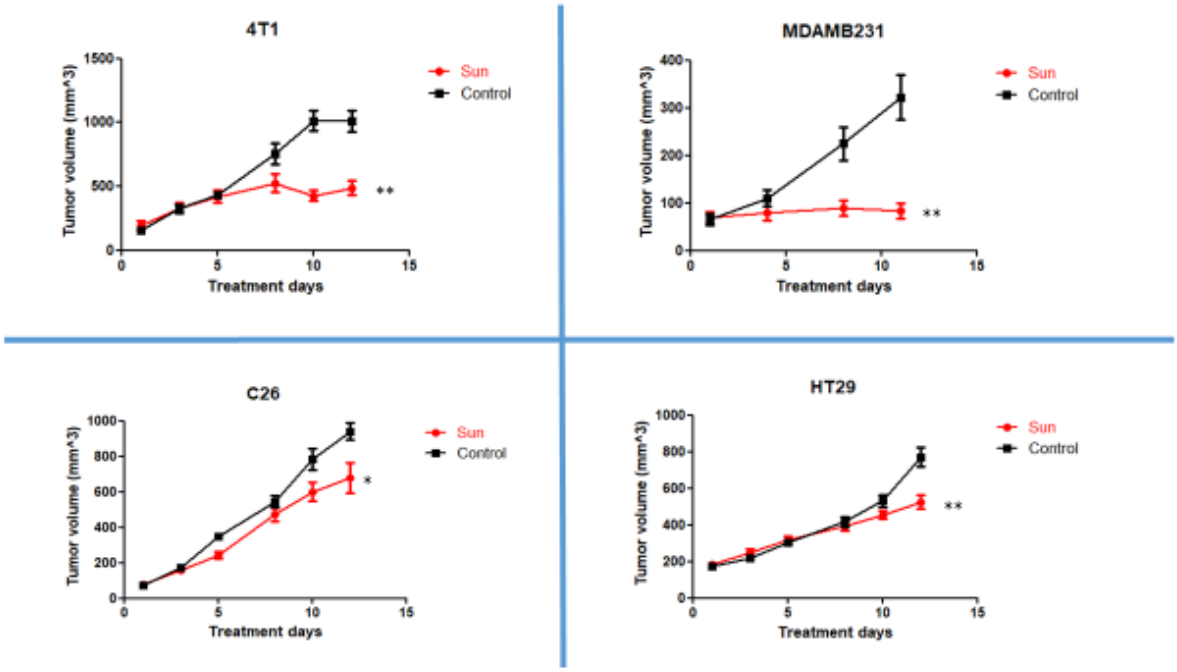

Figure 1. In vivo growth inhibition of sunitinib in different primary tumor models. Growth curves are means for 10 mice per group; bars, SEM.

Moreover, tumor weight (in case of the kidney models tumor containing kidney weight) was also significantly reduced by sunitinib in all primary models as shown in Figure 2. (4T1: p=0,007; MDAMB231: p=0,001; C26: p=0,035; HT29: p=0,0001; RENCA: p=0,0039; Caki-2: p=0,0433).

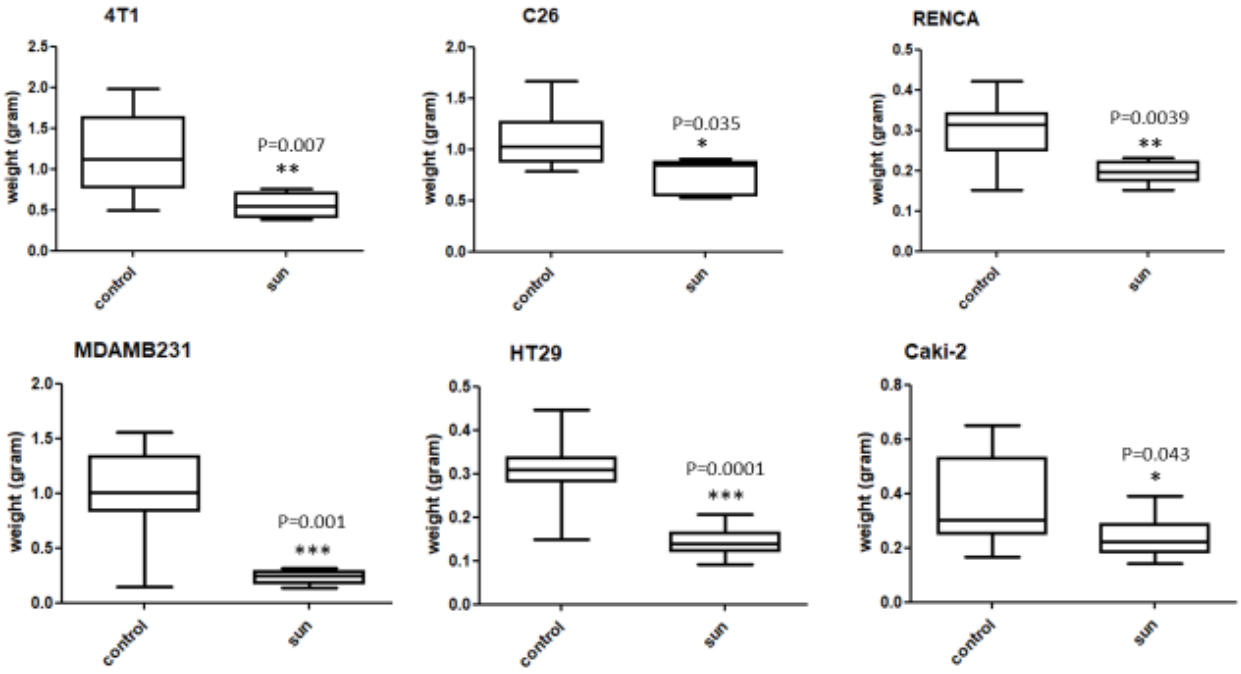

Figure 2. Weight of tumors in different primary tumor models. Data are shown as box (first and third quartiles) and whisker (maximum to minimum) plots with the mean (horizontal bar) from 10 animals per group.

To test the effect of sunitinib treatment on lung metastatis formation of the aforementioned cell lines, cells were inoculated intravenously (iv.) to the tail vein of SCID or Balb/C mice. Metastatic tumor models were generated successfully with the 4T1, MDAMB231, C26 and RENCA cell lines. Treatment of animals begun when tumors reached macroscopic size, and was performed the same way as in the sc. model. As depicted in Figure 3. we found that while antiangiogenic treatment is effective in primary tumor models, it is ineffective for the treatment of lung metastases in all but the RENCA model (4T1: p=0,068; MDAMB231: p=0,606; C26: p=0,9705; HT29: p=0,0028).

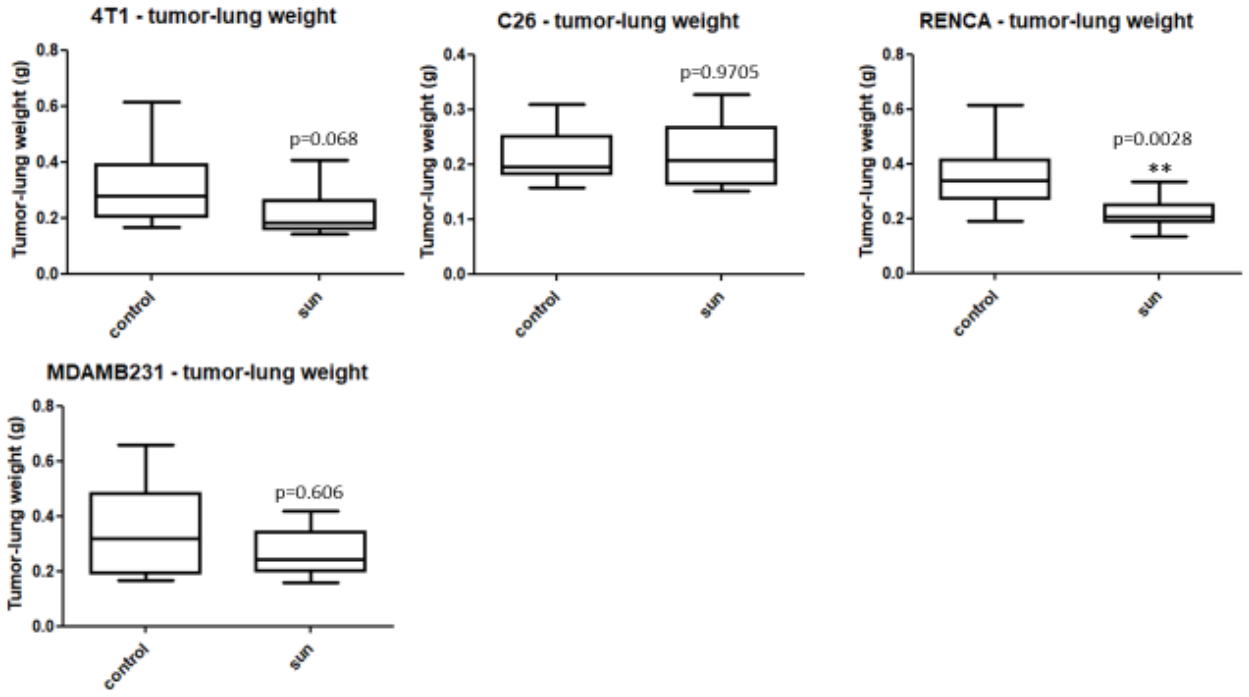

Figure 3. Weights of the lungs in different tumor models of metastatic. Data are shown as box (first and third quartiles) and whisker (maximum to minimum) plots with the mean (horizontal bar) from 10 animals per group.

Serial frozen sections were cut from each tumor. Sections #2 and #5 were used to analyse the distribution and levels of sunitinib by MALDI-MSI and for subsequent haematoxylin&eosin (HE) staining. Section #1 was labeled with anti-caspase 3 antibody, to detect apoptotic cells. For hypoxia detection (section #3), we used the Hypoxyprobe-1 Plus Kit. On section #4 proliferating cells were labelled with anti-BrdU antibody, while on section #6 anti-α-smooth muscle actin (anti-αSMA) was labelled. All sectiones were co-stained with anti-mouse CD31 antibody, followed by a counterstain with Hoechst 33342. Representative images of the aforementioned stainings are shown in Figure 4.

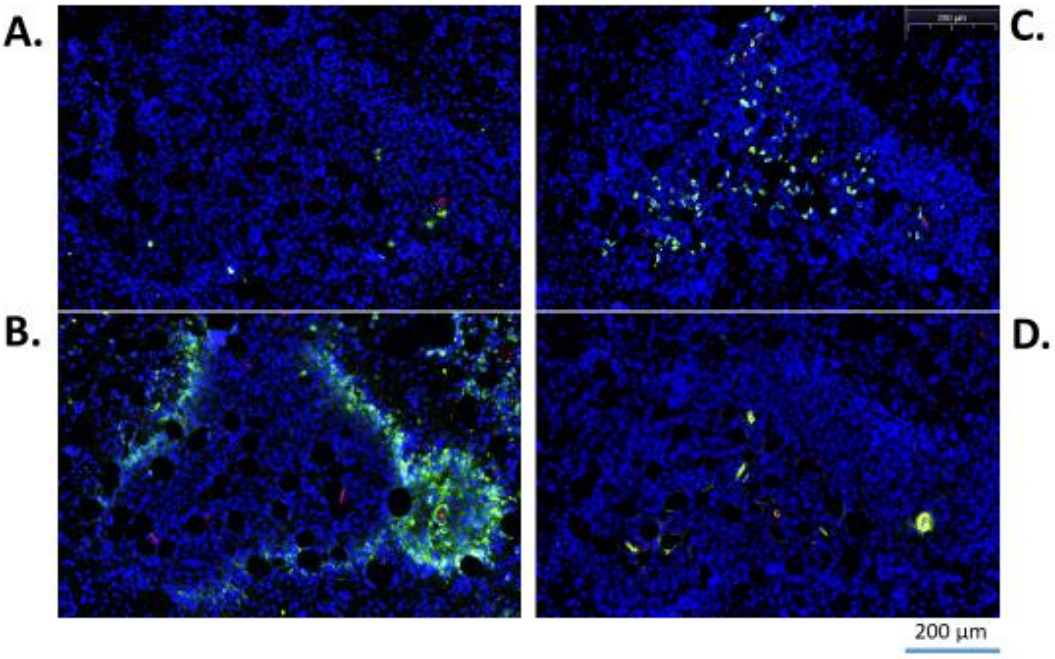

Figure 4. Representative images of A. apoptotic cells labelled with anti-caspase-3 antibody (green); B. hypoxic areas labelled with anti-pimonidazole (green); C. proliferating cells, labelled with anti-BrdU antibody (green); D. staining of anti- αSMA (green). Microvessels are labeled with anti-CD31 (red), and nuclei are stained with Hoechst 33342 (blue) in all sectiones.

Sunitinib distribution and levels were measured by MALDI-MSI as described previously [9]. Dried tissue sectiones were deposited with matrix solution, 7.5 mg/mL α-cyano-4-hydroxycinnamic acid dissolved in 50% acetonitrile and 0.1% trifluoroacetic acid. Heavy (deuterium-labeled analog of sunitinib) sunitinib was added to the matrix solution to serve as an internal standard. Representative images of sunitinib relative signal intensities and distributions are shown in Figure 5.

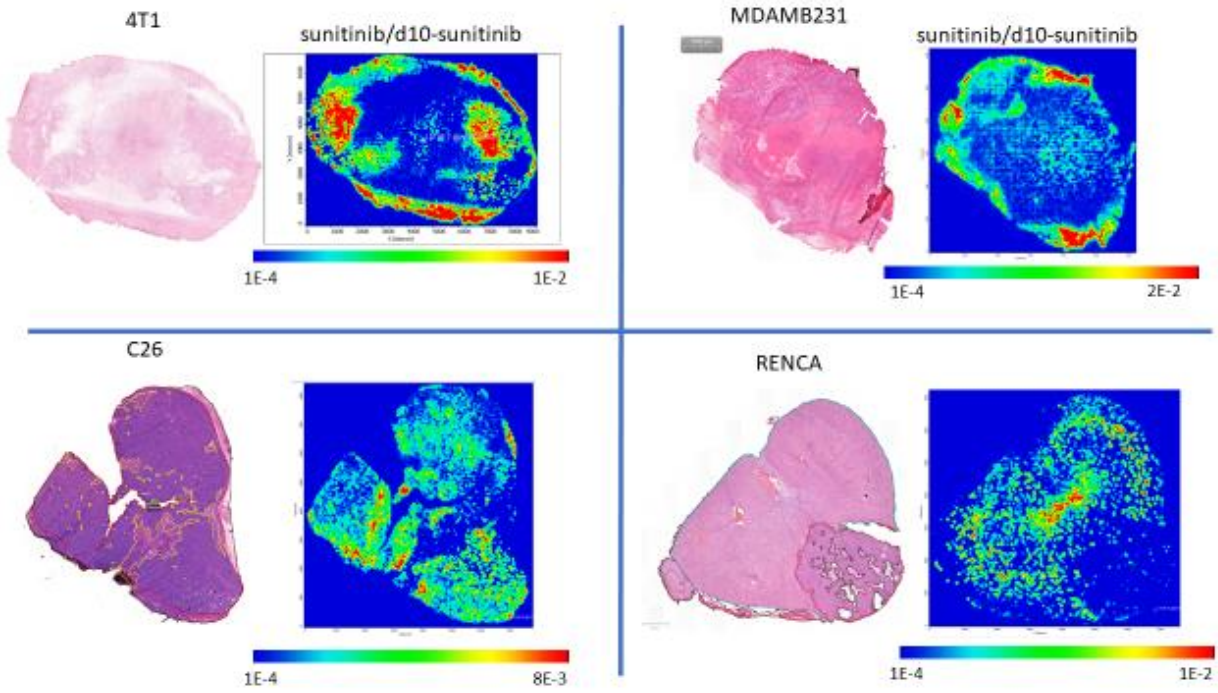

Figure 5. Representative images of sunitinib distribution in 4T1, MDAMB231, C26, RENCA tumor models. Precursor ion signals of sunitinib were normalized to TIC.

To discriminate tumorous and normal tissue manual annotation of tumorous areas were performed. Representative images of the process of annotation and analyzation of sunitinib signal intensities with regards to tumorous-non-tumorous areas are shown in Figure 6.

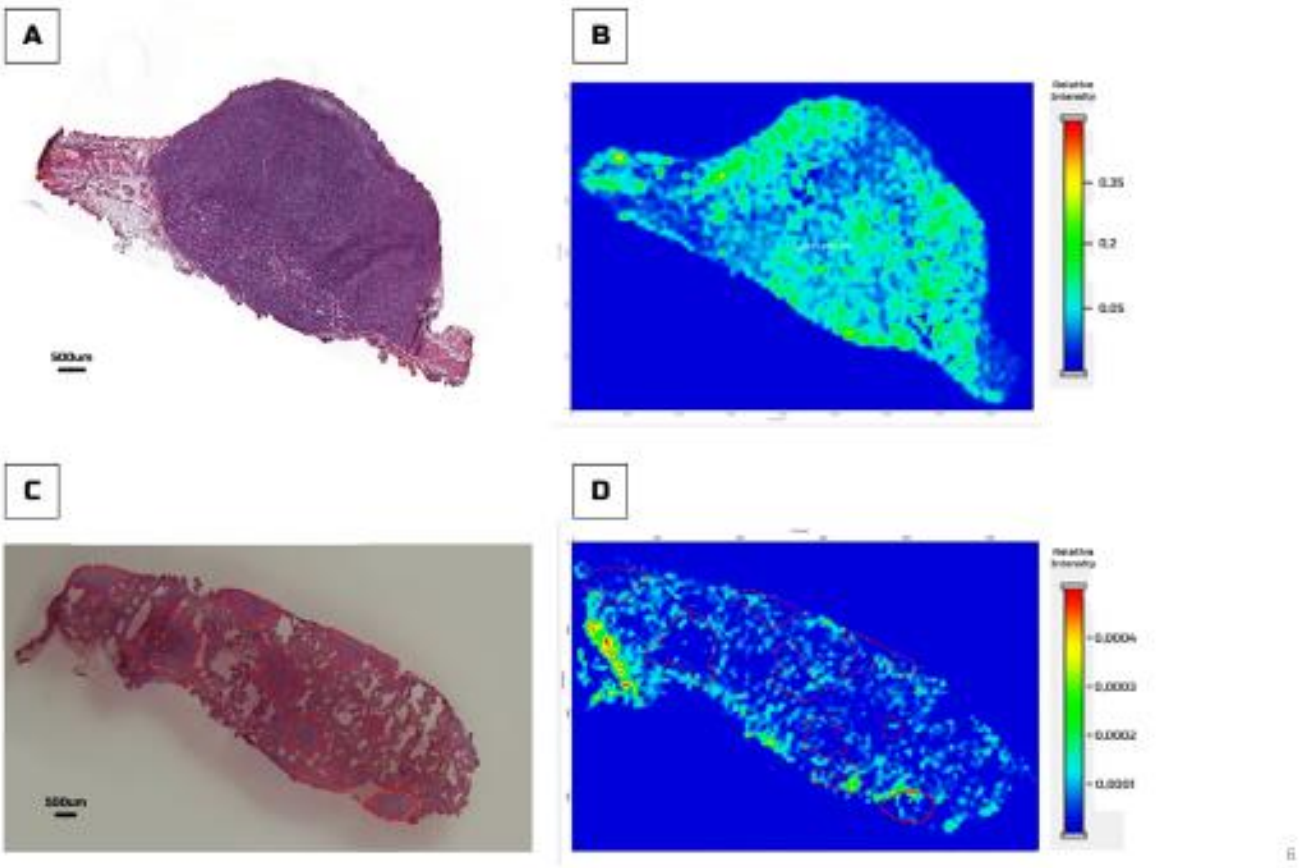

Figure 6. Representative images of primary and metastatic tumor samples of 4T1. HE stained section of primary 4T1 tumor (A.) with sunitinib distribution and levels measured by MALDI-MSI on the same section (B.). HE staines section of metastatic 4T1 tumors in the lung (C.) with sunitinib distribution and levels measured by MALDI-MSI on the same section (D.).

Summary

In our project we successfully generated primary tumor models with the following cell lines: breast cancer 4T1 (mouse)- MDAMB231 (human), colon cancer: C26 (mouse)- HT29 (human), kidney cancer: RENCA (mouse)- CAKI-2 (human). AA treatment resulted in significant tumor growth inhibition when comparing either the the volume or the weight of control and sunitinib treated tumors. Metastatic tumor models were generated successfully with the 4T1, MDAMB231, C26 and RENCA cell lines. While AA treatment was effective in all primary tumor models, it was ineffective for the treatment of lung metastases in all but the RENCA model. We successfully labelled frozen tissue sectiones to detect microvessels, apoptotic cells, hypoxia, proliferating cells and αSMA. Moreover, we were also able to determine tissue distribution and level of sunitinib by MALDI-MSI. Altogether, our results suggest that primary and metastatic tumors differentially respond to AA therapy.

References.

1. Dome, B., et al., *Alternative vascularization mechanisms in cancer: Pathology and therapeutic implications.* Am J Pathol, 2007. **170**(1): p. 1-15.
2. Bugyik, E., et al., *Lack of angiogenesis in experimental brain metastases.* J Neuropathol Exp Neurol, 2011. **70**(11): p. 979-91.
3. Bugyik, E., et al., *Mechanisms of vascularization in murine models of primary and metastatic tumor growth.* Chin J Cancer, 2016. **35**: p. 19.
4. Szabo, V., et al., *Mechanism of tumour vascularization in experimental lung metastases.* J Pathol, 2015. **235**(3): p. 384-96.
5. Pezzella, F., et al., *Non-small-cell lung carcinoma tumor growth without morphological evidence of neo-angiogenesis.* Am J Pathol, 1997. **151**(5): p. 1417-23.
6. Pezzella, F., et al., *Angiogenesis in primary lung cancer and lung secondaries.* Eur J Cancer, 1996. **32A**(14): p. 2494-500.
7. Bridgeman, V.L., et al., *Vessel co-option is common in human lung metastases and mediates resistance to anti-angiogenic therapy in preclinical lung metastasis models.* J Pathol, 2017. **241**(3): p. 362-374.
8. Torok, S., et al., *Limited Tumor Tissue Drug Penetration Contributes to Primary Resistance against Angiogenesis Inhibitors.* Theranostics, 2017. **7**(2): p. 400-412.
9. Torok, S., et al., *Localization of sunitinib, its metabolites and its target receptors in tumour-bearing mice: a MALDI-MS imaging study.* Br J Pharmacol, 2015. **172**(4): p. 1148-63.